A ONE-DIMENSIONAL SIMULATION OF THE STRATOCUMULUS-CAPPED MIXED LAYER

CHAING CHEN and WILLIAM R. COTTON

Department of Atmospheric Science, Colorado State University, Fort Collins, Co. 80523, U.S.A.

(Received in final form 16 December, 1982)

Abstract. A marine stratocumulus model has been developed which has four major sub-models: (1) a one-dimensional version of the CSU cumulus model, (2) a partially-diagnostic higher-order turbulence model, (3) an atmospheric radiation model for both short-wave and long-wave radiation, and (4) a partial condensation scheme and cloud fractional parameterization.

A set of numerical experiments have been performed to study the interactions among the turbulence, the long-wave radiation, the short-wave radiation, and the sub-grid condensation processes. The results indicate that surface sensible eddy heat flux and not radiative cooling is the major control on the rate of cloud-top entrainment. Cloud-top radiation cooling occurs principally within the upper part of the mixed layer. However, for the stratocumulus with numerous towers penetrated into the capping inversion, most of the long-wave radiation occurs within the capping inversion. It is found that cloud-top radiation cooling is balanced by turbulence transport of sensible heat from cloud-base levels.

1. Introduction

The formulation and testing of the turbulence model and the sensitivity experiments with the model using Wangara Day 33 data have been discussed by Chen and Cotton (1983). The marine stratocumulus model is an extension of that work by the inclusion of (1) an atmospheric radiation model for both short-wave and long-wave radiative transfer through a clear, fully cloudy or partly cloudy atmosphere and (2) a partial condensation scheme and cloud fractional parameterization. An eventual goal of this modeling work is to use the model or a simplified version of it as a turbulence closure scheme in a three-dimensional mesoscale model of cloud systems. In fact, using a computer package developed at NCAR, the one-dimensional (1D) model described herein is simply a 1D version of the 3D cloud mesoscale model described by Tripoli and Cotton (1982).

Lilly (1968) studied the cloud-capped mixed layer by using a mixed-layer model. As indicated by Deardorff (1980b), Lilly's mixed-layer model has the following assumptions:

(i) the boundary layer is well mixed for the semi-conservative mean variables;

(ii) the capping inversion has negligible thickness;

(iii) the cloud fractional coverage is 100%;

(iv) there is no wind shear;

(v) there is no drizzle;

(vi) the radiative divergence is entirely within the capping inversion;

(vii) a θ_e or θ_w jump must exist across the capping inversion in order to maintain the stratocumulus cloud layer;

(viii) the mixed-layer model is closed by either the maximum or the minimum entrainment rates at the top of the mixed layer.

Boundary-Layer Meteorology **25** (1983) 289–321. 0006–8314/83/0253–0289$04.95.

From the energy budget of turbulence kinetic energy of the mixed layer, neither the maximum nor the minimum entrainment rate is reasonable. Schubert *et al.* (1979) modified assumptions (viii) by assuming a linear interpolation of the maximum and minimum entrainment rate. Deardorff (1980b) further investigated the cloud-capped mixed layer by using his three-dimensional model. In this paper we will attack the same problem using a one-dimensional model accompanied with a detailed radiation parameterization and sub-grid condensation scheme.

According to the analysis work reported by Noonkester (1979), the evolution of marine stratocumulus is sensitive to radiative cooling and warming. In order to obtain the exact profile of the radiative flux in the atmosphere, one may solve the monochromatic radiation transfer equations separately. The total flux can be calculated by the integration over the whole spectrum. It is obvious that this integration method will put a heavy burden on a computer. Therefore, some parameterizations are adopted to represent the radiation transfer process in the atmosphere.

The radiation model consists of two parts: short-wave and long-wave radiation. The parameterization of long-wave radiation flux through a clear atmosphere follows Rodgers (1967). Because of the presence of cloud, however, Rodgers' clear-air emissivity approach is no longer valid. Stephens (1978) solved this problem by introducing the 'effective' emissivity of the cloud, where the cloud-layer emissivity is parameterized from observations. For the emissivity of an air column containing a clear and cloudy atmosphere (or a partially cloudy atmosphere), Herman and Goody's (1976) 'mixed-emissivity' assumption is adopted.

The short-wave radiation model includes atmospheric molecular scattering, Lacis and Hansen's (1974) ozone absorption, and Stephens' (1978) parameterization of reflectance, transmittance and absorptance of a cloud layer. The structure of the short-wave radiation model follows that of Stephens and Webster (1979), which is a two-stream model (upward and downward flux). Stephens' (1977) 'equivalent transmittance' is employed to derive the reflectance, transmittance and absorptance of a 'clear-cloud mixed' atmosphere.

Because Stephens' parameterization of short-wave radiation through a cloud layer can be 'tuned' to match the results from a detailed theoretical model, one can be more confident of its quantitative value. The exact profile of the radiative variables – reflectance, transmittance and absorptance of a cloud layer – is important to the diurnal evolution of a stratocumulus. This is because the 'penetrative distance' by the short-wave radiation is determined by the above-mentioned radiative variables. The simulation of summer-time Arctic stratus (Herman and Goody, 1976) shows that the penetration of short-wave radiation into the cloud is the source of heating which leads to the formation of two separate cloud layers. However, for a high water content cloud, the penetrative distance is very shallow.

The 'all or nothing' condensation scheme is replaced by a 'partial condensation' parameterization. We adopt a scheme which is similar to Banta and Cotton (1980). The basic assumption of this scheme is that the variable $r - r_s$ is distributed according to a probability density function. The variables r and r_s represent the total water mixing ratio and the saturation mixing ratio. Two types of probability density function are tested:

(1) uniform distribution function (Banta and Cotton, 1980), and (2) skewed distribution function (Bougeault, 1981). Lenschow (personal communication) points out that at the top of the stratus, the cloud top is usually very wavy. Thus the layer near the cloud top may become subsaturated after horizontal averaging. The traditional all or nothing condensation scheme cannot adequately treat this situation. Based on sensitivity experiments, the scheme with a uniform distribution function does not provide a satisfactory result either. The advantage of Bougeault's skewed distribution function is that early condensation occurs at a subsaturated condition. However, the sensitivity experiment also indicates that Bougeault's positively skewed distribution function cannot diagnose the partly cloudy coverage near the cloud top. Thus, the exact formulation of the distribution function near the cloud top will require further investigation.

The primary objectives of this study are:

(i) To compare our one-dimensional model results with Deardorff's (1980b) results which are derived from a three-dimensional model.

(ii) To examine Lilly's (1968) hypothesis that radiation is entirely within the capping inversion.

(iii) To understand the mechanisms that balance cloud-top radiation cooling.

(iv) To determine if cloud-top radiation enhances the entrainment rate.

In Section 2, a detailed description of the model is given. In Sections 3 and 4, the long-wave radiation model and the short-wave radiation model is introduced, respectively. The partial condensation scheme is discussed in Section 5. In the last section, four case studies are compared.

2. Description of the Turbulence Model

The marine stratocumulus-capped mixed layer can be described by the following ensemble-averaged equations.

$$\frac{\partial \bar{u}}{\partial t} = f\bar{v} - f\bar{v}_g + \frac{\partial}{\partial z}(-\overline{u''w''}) - \bar{w}\frac{\partial \bar{u}}{\partial z} \tag{1}$$

$$\frac{\partial \bar{v}}{\partial t} = -f\bar{u} + f\bar{u}_g + \frac{\partial}{\partial z}(-\overline{v''w''}) - \bar{w}\frac{\partial \bar{v}}{\partial z} \tag{2}$$

$$\frac{\partial \bar{\theta}_{il}}{\partial t} = -\bar{w}\frac{\partial}{\partial z}\bar{\theta}_{il} - \frac{\partial}{\partial z}(\overline{w''\theta''_{il}}) - \frac{1}{\rho_0 c_p}\frac{\partial F}{\partial z} \tag{3}$$

$$\frac{\partial \bar{r}}{\partial t} = -\bar{w}\frac{\partial}{\partial z}\bar{r} - \frac{\partial}{\partial z}(\overline{w''r''}) \tag{4}$$

where the variables $(\bar{u}, \bar{v}, \bar{w})$ are the ensemble-averaged wind in the (x, y, z) direction. The variables $(\bar{u}_g, \bar{v}_g)$ are the geostrophic wind in the (x, y) direction. The coriolis parameter is represented by f. The atmospheric radiative cooling or heating rate is

represented by the radiational flux divergence $(-(1/\rho_0 c_p)\ (\partial F/\partial z))$. F is the total radiation flux defined by $F = F\uparrow - F\downarrow$, where $F\uparrow$ and $F\downarrow$ represent upward and downward flux, respectively. ρ_0 is the reference state air density. Equations (1) and (2) can be derived from the equations of motion. In the derivation, the velocity field is decomposed into ensemble-averaged mean and perturbation. $u_i = \bar{u}_i + u_i''$. u_i'' represents the small-scale fluctuations. The thermodynamic variables can also be decomposed into $\theta_{il} = \bar{\theta}_{il} + \theta_{il}''$; $r = \bar{r} + r''$, where θ_{il} and r are ice-liquid water potential temperature and total water mixing ratio, respectively. A double superscript prime notation is used for turbulent fluctuations since in the 3D parent model (see Tripoli and Cotton, 1982) a single prime represents an average departure from the reference state.

In order to close Equations (1) to (4), we need to determine the turbulent flux terms, such as $\overline{u''w''}$, $\overline{v''w''}$, $\overline{w''\theta_{il}''}$, and $\overline{w''r''}$. The detailed description of the formulation of the higher-order turbulence model can be seen in the companion paper (Chen and Cotton, 1983). The turbulent fluxes or the Reynold's stress equations and other second-order moment equations are expressed as:

$$\frac{\partial}{\partial t}\bar{e} = -\bar{w}\frac{\partial}{\partial z}\bar{e} - 2\overline{u_i''w''}\frac{\partial}{\partial z}u_i - \frac{\partial}{\partial z}\left(\overline{u_i''u_i''w''} + \tfrac{4}{3}\frac{1}{\rho_0}\overline{p''w''}\right) + \frac{1}{\rho_0}\left(2\overline{\frac{\partial p''}{\partial x_i}u_i''} - \tfrac{4}{3}\frac{\partial}{\partial z}\overline{p''w''}\right) - \tfrac{4}{3}\bar{\varepsilon}; \qquad i = 1\text{–}2 \tag{5}$$

$$\frac{\partial}{\partial t}\overline{w''^2} = -\bar{w}\frac{\partial}{\partial z}\overline{w''^2} - 2\overline{w''^2}\frac{\partial}{\partial z}\bar{w} - \frac{2g}{\rho_0}\overline{\rho''w''} - \frac{\partial}{\partial z}\left(\overline{w''^3} + \tfrac{2}{3}\frac{1}{\rho_0}\overline{p''w''}\right) + \frac{1}{\rho_0}\left(2\overline{\frac{\partial p''}{\partial z_i}w''} - \tfrac{2}{3}\frac{\partial}{\partial z}\overline{p''w''}\right) - \tfrac{2}{3}\bar{\varepsilon} \tag{6}$$

$$\frac{\partial}{\partial t}\overline{a''^2} = -\bar{w}\frac{\partial}{\partial z}\overline{a''^2} - 2\overline{w''a''}\frac{\partial}{\partial z}\bar{a} - \frac{\partial}{\partial z}\overline{w''a''^2} - 2\bar{\varepsilon}_{aa} \tag{7}$$

$$\frac{\partial}{\partial t}\overline{a''b''} = -\bar{w}\frac{\partial}{\partial z}\overline{a''b''} - \overline{w''a''}\frac{\partial}{\partial z}\bar{b} - \overline{w''b''}\frac{\partial}{\partial z}\bar{a} - \frac{\partial}{\partial z}\overline{w''a''b''} - 2\bar{\varepsilon}_{ab} \tag{8}$$

$$\frac{\partial}{\partial t}\overline{u_i''w''} = -\bar{w}\frac{\partial}{\partial z}\overline{u_i''w''} - 2\overline{u_i''w''}\frac{\partial}{\partial z}\bar{w} - \overline{w''^2}\frac{\partial}{\partial z}\bar{u}_i - \frac{\partial}{\partial z}\overline{u_i''w''^2} - \frac{g}{\rho_0}\overline{\rho''u_i''} + \frac{1}{\rho_0}\left(\overline{\frac{\partial p''}{\partial x_i}w''} + \overline{\frac{\partial p''}{\partial z}u_i''}\right); \qquad i = 1\text{–}2 \tag{9}$$

$$\frac{\partial}{\partial t}\overline{w''a''} = -\bar{w}\frac{\partial}{\partial z}\overline{w''a''} - \overline{w''a''}\frac{\partial}{\partial z}\bar{w} - \overline{w''^2}\frac{\partial}{\partial z}\bar{a} - \frac{\partial}{\partial z}\overline{w''^2 a''}$$

$$-\frac{g}{\rho_0}\overline{\rho''a''} + \frac{1}{\rho_0}\overline{\frac{\partial p''}{\partial z}a''} \tag{10}$$

$$\overline{u''v''}\left(\frac{\partial \bar{w}}{\partial z} + \frac{c_1}{\tau}\right) = -\overline{u''w''}\frac{\partial}{\partial z}\bar{v} - \overline{v''w''}\frac{\partial}{\partial z}\bar{u} \tag{11}$$

$$\overline{u_i''a''}\,(c_0/\tau) = -\overline{u_i''w''}\frac{\partial}{\partial z}\bar{a} - \overline{w''a''}\frac{\partial}{\partial z}\bar{u}_i\,; \quad i = 1 - 2. \tag{12}$$

where $\bar{e}$ is defined as $\overline{u''^2} + \overline{v''^2}$. The scalars a and b represent either θ_{il} or r. The isotropy terms represent the corelations between pressure fluctuation (p'') and velocity (u_i'') or pressure fluctuation and thermodynamic variables (r'', θ_{il}) and are parameterized following Zeman and Lumley (1976) as:

$$\frac{1}{\rho_0}\left(\overline{\frac{\partial p''}{\partial x_i}u_k''} + \overline{\frac{\partial p''}{\partial x_k}u_i''} - \frac{2}{3}\delta_{ik}\frac{\partial}{\partial z}\overline{p''w''}\right) =$$

$$\frac{c_1}{\tau}b_{ik}q^2 - \frac{3}{10}R_1(\overline{u_i''\theta_{il}''}\,\delta_{3k} + \overline{u_k''\theta_{il}''}\,\delta_{3i} - \tfrac{2}{3}\overline{w''\theta_{il}''}\,\delta_{ik})$$

$$-\frac{3}{10}R_2(\overline{u_i''r''}\,\delta_{3k} + \overline{u_k''r''}\,\delta_{3i} - \tfrac{2}{3}\overline{w''r''}\,\delta_{ik}) \tag{13}$$

$$-\frac{3}{10}R_3(\overline{u_i''r_c''}\,\delta_{3k} + \overline{u_k''r_c''}\,\delta_{3i} - \tfrac{2}{3}\overline{w''r_c''}\,\delta_{ik})$$

$$-\frac{1}{\rho_0}\overline{\frac{\partial p''}{\partial z}a''} = \frac{c_0}{\tau}\overline{w''a''} - \tfrac{1}{3}(R_1\overline{\theta_{il}''a''} + R_2\overline{r''a''} + R_3\overline{r_c''a''}) \tag{14}$$

where $b_{ik} = \overline{u_i''u_k''}/q^2 - \frac{1}{3}\delta_{ik}$ and q^2 is defined by $q^2 = \overline{u''u''} = \bar{e} + \overline{w''^2}$, $c_1 = 1.0$, $c_0 = 2.17$. τ is the turbulence time scale for the second-order moments, which is defined by $\tau = \mu q^2/\bar{\varepsilon}$, $\mu = 0.31$, $\bar{\varepsilon}$ is the mean rate of turbulence energy dissipation. By the same token, $\bar{\varepsilon}_{ab}$ represents the mean destruction rate of $\overline{a''b''}$, i.e., the destruction of $\overline{\theta_{il}''^2}$, $\overline{r''^2}$, or $\overline{\theta_{il}''r''}$. $\bar{\varepsilon}_{ab}$ is defined by $\bar{\varepsilon}_{ab} = \mu\overline{a''b''}/\tau_0$ where τ_0 is the turbulence time scale for all thermodynamic variables. Equations (6), (9), and (10) have a term which is the correlation between density fluctuation ρ'' and other turbulence variables. The covariance with density fluctuations ρ'' can be written as:

$$\frac{-g\overline{\rho''\alpha''}}{\rho_0} = -R_1\overline{\theta_{il}''\alpha''} - R_2\overline{r''\alpha''} - R_3\overline{r_c''\alpha''} \tag{15}$$

where α'' can be any turbulent fluctuation. The coefficients R_1, R_2, and R_3 are given by

$$R_1 = -g/\theta_0$$
$$R_2 = -(R_v/R_a - 1)g \tag{16}$$
$$R_3 = -(L_{lv}/c_p T_0 - R_v/R_a)g$$

where the subscript '0' denotes the reference state and R_a, R_v are the gas constants for dry air and water vapor. L_{lv} is the latent heat of evaporation.

The above second-order moment equations are closed with third-order moment equations. The procedure to parameterize the third-order moments follows Chen and Cotton (1983), which is an extension of the model originally developed by Zeman and Lumley (1976). The following equations are a summary of all the third-order moment equations.

$$\overline{w''a''b''}\left(\frac{1}{\tau_3}+\frac{2\mu}{\tau_0}\right) = -\overline{w''^2}\frac{\partial}{\partial z}\overline{a''b''} - \overline{w''a''}\frac{\partial}{\partial z}\overline{w''b''} - \overline{w''b''}\frac{\partial}{\partial z}\overline{w''a''}$$
$$-R_1\,\overline{\theta_{il}''a''b''} - R_2\,\overline{r''a''b''} - R_3\,\overline{r_c''a''b''} \tag{17}$$

$$\overline{w''^2a''}\left(\frac{1}{\tau_3}+\frac{4\mu}{3\tau}\right) = -2\,\overline{w''^2}\frac{\partial}{\partial z}\overline{w''a''} - \overline{w''a''}\frac{\partial}{\partial z}\overline{w''^2}$$
$$-5/3\,(R_1\,\overline{w''\theta_{il}'a''} + R_2\,\overline{w''r''a''} + R_3\,\overline{w''r_c''a''}) \tag{18}$$

$$\overline{q^2w''}\left(\frac{1}{\tau_3}+\frac{4\mu}{3\tau}+\frac{2\mu}{\tau}\right) = (\overline{w''u_i''u_i''})\left(\frac{1}{\tau_3}+\frac{4\mu}{3\tau}+\frac{2\mu}{\tau}\right)$$
$$= -\overline{w''^2}\frac{\partial}{\partial z}\overline{u_i''u_i''} - 2\,\overline{w''u_i''}\frac{\partial}{\partial z}\overline{w''u_i''}$$
$$-3\,(R_1\,\overline{w''^2\theta_{il}''} + R_2\,\overline{w''^2r''} + R_3\,\overline{w''^2r_c''}) \tag{19}$$

$$\overline{u_i''w''^2}\left(\frac{1}{\tau_3}+\frac{4\mu}{3\tau}\right) = -\overline{u_i''w''}\frac{\partial}{\partial z}\overline{w''^2} - 2\,\overline{w''^2}\frac{\partial}{\partial z}\overline{u_i''w''}\;;\quad i = 1-2. \tag{20}$$

Equation (17) represents the diagnostic equation for $\overline{w''r''^2}$, $\overline{w''\theta_{il}''^2}$, and $\overline{w''\theta_{il}''r''}$. Equation (18) represents the equation for $\overline{w''^2r''}$ and $\overline{w''^2\theta_{il}''}$. Equation (20) is the diagnostic equation for $\overline{u''w''^2}$ and $\overline{v''w''^2}$. In order to have a reasonable redistribution of energy among $\overline{w''^3}$, $\overline{u''^2w''}$, and $\overline{v''^2w''}$, we use a simple approximation that

$$\overline{w''^3} = \tfrac{1}{2}\,\overline{q^2w''},\quad \overline{u''^2w''} = \overline{v''^2w''} = \tfrac{1}{2}\,\overline{w''^3}. \tag{21}$$

The skewness terms $\overline{\theta_{il}''^3}$, $\overline{\theta_{il}''^2r''}$, $\overline{\theta_{il}''r''^2}$, and $\overline{r''^3}$ are described as follows:

$$\overline{\theta_{il}''^3}\left(1-\frac{3\tau_0}{2\mu}\frac{R_1}{A_1}\frac{\partial\overline{\theta_{il}}}{\partial z}\right) = -\frac{3\tau_0}{2\mu}\left(\overline{w''\theta_{il}'}\frac{\partial}{\partial z}\overline{\theta_{il}''^2} + \frac{B_1}{A_1}\frac{\partial\overline{\theta_{il}}}{\partial z}\right) \tag{22}$$

$$\overline{\theta_{il}''^2 r''}\left(1-\frac{\tau_0}{\mu}\frac{R_1}{A_1}\frac{\partial\overline{\theta_{il}}}{\partial z}\right)=-\frac{\tau_0}{2\mu}\left(\overline{w''r''}\frac{\partial}{\partial z}\overline{\theta_{il}''^2}+2\,\overline{w''\theta_{il}}\frac{\partial}{\partial z}\overline{\theta_{il}''r''}\right)$$
$$-\frac{\tau_0}{2\mu}\frac{\partial\bar{r}}{\partial z}\left(\frac{B_1}{A_1}-\frac{R_1}{A_1}\overline{\theta_{il}''^3}\right)-\frac{\tau_0}{\mu}\frac{C_1}{A_1}\frac{\partial\overline{\theta_{il}}}{\partial z} \tag{23}$$

$$\overline{\theta_{il}''r''^2}\left(1-\frac{\tau_0}{2\mu}\frac{R_1}{A_1}\frac{\partial\overline{\theta_{il}}}{\partial z}\right)=-\frac{\tau_0}{2\mu}\left(\overline{w''\theta_{il}''}\frac{\partial}{\partial z}\overline{r''^2}+2\,\overline{w''r''}\frac{\partial}{\partial z}\overline{\theta_{il}''r''}\right)$$
$$-\frac{\tau_0}{2\mu}\frac{D_1}{A_1}\frac{\partial\overline{\theta_{il}}}{\partial z}-\frac{\tau_0}{\mu}\frac{C_1}{A_1}\frac{\partial\bar{r}}{\partial z}+\frac{\tau_0}{\mu}\frac{R_1}{A_1}\frac{\partial\bar{r}}{\partial z}\overline{\theta_{il}''^2 r''} \tag{24}$$

$$\overline{r''^3}=-\frac{3\tau_0}{2\mu}\overline{w''r''}\frac{\partial}{\partial z}\overline{r''^2}-\frac{3\tau_0}{2\mu}\frac{\partial\bar{r}}{\partial z}\left(\frac{D_1}{A_1}-\frac{R_1}{A_1}\overline{\theta_{il}''r''^2}\right) \tag{25}$$

where

$$A_1=\frac{1}{\tau_3}+\frac{2\mu}{\tau_0} \tag{26}$$

$$B_1=-\overline{w''^2}\frac{\partial}{\partial z}\overline{\theta_{il}''^2}-2\overline{w''\theta_{il}''}\frac{\partial}{\partial z}\overline{w''\theta_{il}''} \tag{27}$$

$$C_1=-\overline{w''^2}\frac{\partial}{\partial z}\overline{\theta_{il}''r''}-\overline{w''\theta_{il}''}\frac{\partial}{\partial z}\overline{w''r''}-\overline{w''r''}\frac{\partial}{\partial z}\overline{w''\theta_{il}''} \tag{28}$$

$$D_1=-\overline{w''^2}\frac{\partial}{\partial z}\overline{r''^2}-2\overline{w''r''}\frac{\partial}{\partial z}\overline{w''r''}. \tag{29}$$

In the companion paper (Chen and Cotton, 1983), we have compared the parameterizations of dissipation given by André *et al.* (1978) and Sun and Ogura (1980). As a consequence of the results of that study, we adopt André's scheme which can be summarized as follows.

The dissipation of turbulence kinetic energy is defined by

$$\bar{\varepsilon}=0.31q^3/l \tag{30}$$

where l is the turbulence length scale which is defined by

$$l=\text{MIN}\,(l_B, l_D) \tag{31}$$

where l_B is the Blackadar's length scale for the surface related unstable layer:

$$l_B=kz/(1+kz/l_0) \tag{32}$$

l_0 is the characteristic length scale

$$l_0 = 0.1 \frac{\int qz \, dz}{\int q \, dz}. \tag{33}$$

The coefficient $k = 0.35$ is the Von Karman constant. As for the stable stratification near the top of the mixed layer, the associated length scale is parameterized by l_D, where

$$l_D = 0.75 \left[q^2/2/\left(-R_1 \frac{\partial}{\partial z} \overline{\theta_{il}} \right) \right]^{1/2}. \tag{34}$$

The turbulence time scale can then be defined by $\tau = \mu q^2/\bar{\varepsilon}$. From the discussion mentioned in the companion paper, τ_0 and τ_3 are defined by

$$\tau_0 = \tau/2, \quad \tau_3 = \tau/2.17.$$

Furthermore, $\bar{\varepsilon}_0$, $\bar{\varepsilon}_r$, and $\bar{\varepsilon}_{0r}$ can be parameterized as

$$\begin{aligned} \bar{\varepsilon}_0 &= \frac{\mu \overline{\theta_{il}''^2}}{\tau_0} \\ \bar{\varepsilon}_r &= \frac{\mu \overline{r''^2}}{\tau_0} \\ \bar{\varepsilon}_{0r} &= \mu \, \overline{\theta_{il}'' r''}/\tau_0. \end{aligned} \tag{35}$$

With the atmospheric radiation model activated, radiation cooling may occur at cloud top and radiation warming at cloud base. The radiative flux divergence can thus produce a convectively unstable layer inside the cloud layer. Blackadar's formulation is not applicable to these conditions since the source of convective instability is not heat flux from the earth's surface, but is diabatic heating within the mixed layer.

We therefore adopt the following formulation inside the cloud layer when $\overline{\partial \theta_{il}}/\partial z < 0$. The turbulence scale is then defined as

$$\tau = \overline{w''^2}/B \tag{36}$$

where B is the buoyancy production of turbulence kinetic energy, which can be expressed as

$$B = -2(R_1 \, \overline{w'' \theta_{il}''} + R_2 \, \overline{w'' r''} + R_3 \, \overline{w'' r_c''}). \tag{37}$$

We define Equation (36) based on the fact that the buoyancy production of turbulence kinetic energy (B) is always a dominant term. Dissipation therefore should always adjust to B. Equation (36) indicated that the dissipation is about 60% of B. Kaimal *et al.* (1976) found that the mid-layer dissipation rate is about 0.4–0.5 times the buoyant production rate.

3. Long-Wave Radiation Model

3.1. Radiative transfer equation

The radiative transfer equation (RTE) can be expressed in the integral form, i.e.,

$$F(p') = F(p_0)\left[1 - \int_{p_0}^{p'} \frac{\partial \varepsilon}{\partial p}\,\mathrm{d}p\right] + \int_{p_0}^{p'} \sigma T^4(p)\frac{\partial \varepsilon}{\partial p}\,\mathrm{d}p \tag{38}$$

where $F(p_0)$ is the long-wave radiative flux at the boundary p_0, ε is the emissivity, the variable p denotes pressure, σT^4 represents the source function of the long-wave radiative flux which is Stefan-Boltzmann black-body radiation.

The above mentioned RTE can be converted to the following form when it is applied to a grid-point model,

$$F(N) = F(1)\,(1 - \bar{\varepsilon}_N) + \sum_{k=1}^{N-1} \sigma T_{k+1/2}^4\,\Delta\bar{\varepsilon}_{k+1/2} \tag{39}$$

where k denotes the number of layers, and the outmost layer is denoted by N. $\bar{\varepsilon}_N$ is the total emissivity of the combined layers (k = 1 to N). $\bar{\varepsilon}_N$ can be expressed by

$$\bar{\varepsilon}_N = \bar{\varepsilon}\left(\sum_{l=1}^{N-1} U_{l+1/2}\right)$$

where $U_{l+1/2}$ is the optical path length between the lth and l + 1th layer. The optical path length is defined by

$$U_{l+1/2} = \rho_0 r_v(z_{l+1/2})\,(z_{l+1} - z_l) \tag{40}$$

where ρ_0 is the density of the air, r_v is the mixing ratio of water vapor. Equation (40) indicates that the optical path length $U_{l+1/2}$ is just the total water vapor content per unit area between the l + 1th and lth layers.

In Equation (39), $\Delta\bar{\varepsilon}_{k+1/2}$ represent the 'actual' emissivity of the $k + \frac{1}{2}$th layer and is defined by

$$\Delta\bar{\varepsilon}_{k+1/2} = \bar{\varepsilon}\left(\sum_{l=k}^{N-1} U_{l+1/2}\right) - \bar{\varepsilon}\left(\sum_{l=k+1}^{N-1} U_{l+1/2}\right). \tag{41}$$

It is important to note that the actual emissivity $\Delta\bar{\varepsilon}_{k+1/2}$ has different values for upward and downward fluxes.

Based on observations, Stephens (1978) formulated the RTE through a cloud layer as

$$\begin{aligned} F_T\uparrow &= F_B\uparrow\,(1 - \bar{\varepsilon}^{\uparrow}_{\mathrm{eff}}) + \bar{\varepsilon}^{\uparrow}_{\mathrm{eff}}\,\sigma T^4 \\ F_B\downarrow &= F_T\downarrow\,(1 - \bar{\varepsilon}^{\downarrow}_{\mathrm{eff}}) + \bar{\varepsilon}^{\downarrow}_{\mathrm{eff}}\,\sigma T^4 \end{aligned} \tag{42}$$

where the subscripts T and B denote cloud top and cloud base. The upward and downward emissivities of a cloud layer are denoted as $\bar{\varepsilon}\uparrow_{\text{eff}}$ and $\bar{\varepsilon}\downarrow_{\text{eff}}$, respectively; they are determined from observations and will be discussed in the next two sections.

3.2. Parameterization of Emissivity of a Clear Atmosphere

Rodgers (1967) parameterized the emissivity of a clear atmosphere by a simple algebraic expression of the form.

$$\varepsilon\uparrow\downarrow = \begin{cases} \sum_{n=1}^{4} a_n\uparrow\downarrow \, U^{n/2}, & U \leq 10^{-3} \text{ gm cm}^{-2} \\ \sum_{n=0}^{4} b_n\uparrow\downarrow \, (\ln U)^n, & U > 10^{-3} \text{ gm cm}^{-2} \end{cases} \tag{43}$$

where U is the water vapor optical path length. a_n and b_n are coefficients which are given in Table I, and the arrow direction is either up or down, respectively.

TABLE I

Values of the coefficients in Equation (43)

	a_1	a_2	a_3	a_4	b_0	b_1	b_2	b_3	b_4
↑	9.32	−446.4	824	259700	0.5983	0.15068	3.4041×10^{-2}	6.5535×10^{-3}	4.887×10^{-4}
↓	8.857	−332.8	14607	−261900	0.6558	0.12175	1.4976×10^{-2}	1.4981×10^{-3}	0.49×10^{-4}

Rodgers claims that this emissivity parameterization can give a good solution to the upward and downward radiative flux through a clear atmosphere.

Due to the absorption of water vapor in the 8–13 μm, we correct Rodger's emissivity according to the formulation described by Stephens and Webster (1979). The emissivities calculated by Equation (43) are modified by adding $\varepsilon'\uparrow$ and $\varepsilon'\downarrow$ to the upward and downward emissivities. $\varepsilon'\uparrow$ and $\varepsilon'\downarrow$ are determined by

$$\varepsilon'\uparrow = \sum_{n=0}^{4} a'_n \left[\log_e (U P_e)^n\right]$$

$$\varepsilon'\downarrow = \sum_{n=0}^{4} b'_n \left[\log_e (U P_e)^n\right].$$

Where P_e is the ratio of partial water vapor pressure, which can be computed from

$$P_e = \frac{P r_v}{0.622 \times 1013.6}.$$

The variable p denotes pressure. The coefficients a'_n and b'_n are given by Stephens and Webster (1979, Table I).

3.3. Parameterization of emissivity of a cloudy atmosphere

The effective emissivity ($\bar{\varepsilon}_{\text{eff}}\uparrow\downarrow$) of a cloud layer as determined from observations (Stephens, 1978) can be given as follows:

$$\varepsilon\uparrow\downarrow_{\text{eff}} = 1 - \exp(-a_0\uparrow\downarrow W) \tag{44}$$

where W is the liquid water optical path length (g m^{-2}) given by $W = \int \rho_0 r_l \, dz$. $a_0\uparrow$ and $a_0\downarrow$ are coefficients for upward and downward emissivity and are given as

$$a_0\uparrow = 0.13 \quad \text{and} \quad a_0\downarrow = 0.158. \tag{45}$$

3.4. Emissivity of a mixed clear and cloudy atmosphere

In the stratocumulus model, the vertical extended air column contains water vapor, and cloud water. Both Rodgers' and Stephens' emissivity cannot represent the actual emissivity of this volume of air. A simple parameterization used by Herman and Goody (1976) is adopted, which is called 'mixed emissivity'. The mixed emissivity is defined by

$$(1 - \bar{\varepsilon}_m) = (1 - \bar{\varepsilon}_{\text{clear}})(1 - \bar{\varepsilon}_{\text{eff}} H_{\max}) \tag{46}$$

where $\bar{\varepsilon}_m$ is the mixed emissivity. $\bar{\varepsilon}_{\text{clear}}$ and $\bar{\varepsilon}_{\text{eff}}$ are the emissivity for a clear and cloudy atmosphere, respectively. $H_{\max}$ is the maximum cloud fractional coverage of the clear-cloud mixed layers.

Another approach to computing long-wave flux in the 'clear-cloudy mixed' layer is to adopt Stephens' empirical radiative equation if there is a cloud layer. This scheme is not a 'continuous' process when compared to the mixed emissivity approach. However, those two schemes are essentially the same whenever the cloud-water mixing ratio is greater than 1 g kg^{-1}. Differences between those two schemes appear when the cloud-water mixing ratio is less than 1 g kg^{-1}. The differences, however, are very small.

3.5. Boundary conditions for the radiation model

An intermediate layer is placed between the top of the model and the top of the atmosphere in which zero flux is assumed for the downward long-wave flux at the top of the atmosphere. Sensitivity experiments show that the downward long-wave flux at the top of the model is sensitive to the water vapor content and the thermal temperature within the intermediate layer. The total water vapor content of this intermediate layer is assumed to be 0.3 gm cm^{-2}. The thermal temperature is assumed to be the temperature of the layer above the top of the model, because most of the downward long-wave flux at the top of the model is contributed by the black-body radiation from the nearby layers.

4. Short-Wave Radiation Model

4.1. Radiative transfer equation

Once the reflectance, absorptance and transmittance are known for a given layer, a two-stream (upward flux and downward flux) radiative transfer model can be con-

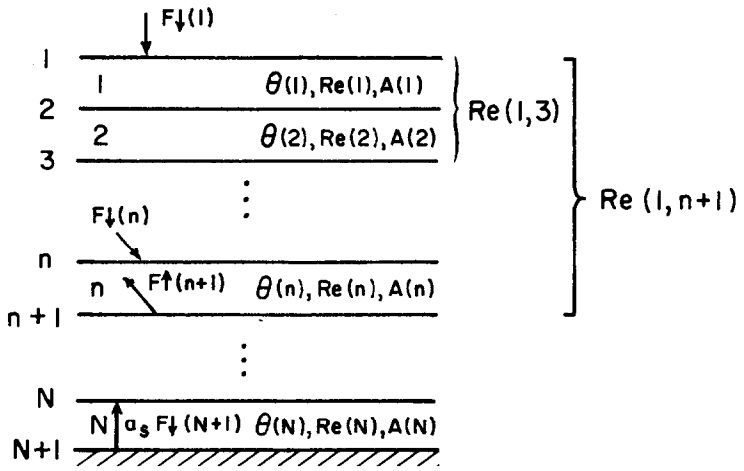

Fig. 1. The short-wave radiative transfer model, $F\downarrow$ and $F\uparrow$ denote downward and upward fluxes. $Re(n)$ and $A(n)$ represent respectively the reflectance, absorptance at the n^{th} layer. $Re(1, n+1)$ is the multiple reflectance from all layers above the $(n+1)$th layer.

structed. Figure 1 (from Stephens and Webster (1979)) represents a simple illustration of such a radiative transfer model. In Figure 1, downward and upward flux are denoted by $F\downarrow$ and $F\uparrow$ respectively and can be written as

$$F\downarrow(n+1) = Re(1, n+1)\, F\uparrow(n+1) + V\downarrow(n+1/2) \tag{47}$$

$$F\uparrow(n) = \frac{Tr\uparrow(n)\, F\uparrow(n+1)}{1 - Re(1, n)\, Re(n)} + V\uparrow(n+1/2) \tag{48}$$

where the number of layers is denoted by n; $Re(n)$, $A(n)$, and $Tr(n)$ represent, respectively, the reflectance, absorptance and transmittance. $Re(1, n+1)$ represents the 'multiple' reflectance from all layers above the $(n+1)$st layer, defined as

$$Re(1, n+1) = Re(n) + \frac{Tr\downarrow(n)\, Tr\uparrow(n)\, Re(1, n)}{1 - Re(1, n)\, Re(n)} \tag{49}$$

The second term on the right-hand side of Equation (49) represents the internal doubling effect between layers (Stephens, 1977).

$V\downarrow(n+\frac{1}{2})$ represents the flux transmitted from the upper layer, computed as

$$V\downarrow(n+\tfrac{1}{2}) = \frac{Tr\downarrow(n)\, V\downarrow(n-1/2)}{1 - Re(1, n)\, Re(n)}. \tag{50}$$

$V\uparrow(n+\frac{1}{2})$ represents the flux transmitted from the lower layer, calculated by

$$V\uparrow(n+\tfrac{1}{2}) = \frac{Re(n)\, V\downarrow(n-\frac{1}{2})}{1 - Re(1, n)\, Re(n)}. \tag{51}$$

The boundary conditions for this short-wave radiative transfer model are:

$$Re(1, 1) = 0$$

$$V\downarrow(\tfrac{1}{2}) = F\downarrow(1)$$

$$F\uparrow(n + 1) = a_s F\downarrow(n + 1)$$

where a_s is the surface albedo. A value of 0.0667 is used for the albedo over the sea surface (Neumann and Pierson, 1966).

4.2. Parameterization of Reflectance, Transmittance and Absorptance

4.2.1. *Parameterization of Absorptance of a Clear Atmosphere*

Similar to the models formulated by Oliver and Lewellen (1978), Lacis and Hansen (1974) and Herman and Goody (1976), we adopt Yamamoto's (1962) parameterization of the absorptance through the clear atmosphere. Thus, the absorptance is defined by

$$A_r(m_z) = 2.9m_z/[(1 + 141.5M\, m_z)^{0.635} + 5.925M\, m_z] \tag{53}$$

where m_z is the optical path length of water vapor above layer z and can be written as

$$m_z = \int_z^\infty \rho_v \, dz = \int_z^\infty \rho_0 r_v \, dz$$

where ρ_v, ρ_0 are the density of water vapor and air, respectively and r_v is the water vapor mixing ratio.

The magnification factor M (Rodgers, 1967) accounts for the slant path and refraction. M is defined by

$$M = 35/(1224\mu_0^2 + 1)^{1/2}$$

when $\mu_0 = \cos\phi$, ϕ is the zenith angle.

There is a limitation to using Equation (53), however. When the atmosphere contains a cloud layer, it is very difficult to evaluate the actual absorptance for a clear-cloud mixed atmosphere. In a later section, a scheme is introduced to parameterize the absorptance for a clear-cloud mixed atmosphere.

4.2.2. *Atmospheric Molecular Scattering*

Most of the atmospheric molecular Rayleigh scattering occurs in the lower atmosphere. When integrated through the atmosphere, the Rayleigh scattering provides a total 7% reflectance in the troposphere which corresponds to the climatological mean reflectance. Stephens (personal communication) parameterizes the atmospheric reflectance of each layer due to Rayleigh scatter as

$$Re_{\text{clear}}(P) = (0.219 \times 0.517)\, P/[1 + 0.816\mu_o) \times 3039 \times 10^3] \tag{54}$$

where P is the pressure.

4.2.3. *The Ozone Absorption*

The parameterization of the absorptance due to ozone absorption in the intermediate layer above the model top follows Lacis and Hansen (1974), and is given by

$$A_{oz}(X_l) = A_{oz}^{uv}(X_l) + A_{oz}^{vis}(X_l) \tag{55}$$

where A_{oz} represents the total absorptance. The optical path length of ozone above the lth layer is denoted by X_l. Superscripts *uv* and *vis* denote the ultraviolet and visual spectral range, respectively. A_{oz}^{uv} and A_{oz}^{vis} can be defined as follows

$$A_{oz}^{uv}(X_l) = \frac{1.082X_l}{(1 + 138.6X_l)^{0.805}} + \frac{0.0658X_l}{1 + (103.6X_l)^3} \tag{56}$$

$$A_{oz}^{vis}(X_l) = \frac{0.02118X_l}{1 + 0.042X_l + 0.000323X_l^2}. \tag{57}$$

4.3. Parameterization of Reflectance, Transmittance and Absorptance of a Cloud Layer

In order to model the specular variation due to the main short-wave absorbers in the atmosphere (i.e., water, ozone and carbon dioxide), Stephens (1978) parameterized the reflectance, transmittance and absorptance of a cloud layer by considering two bands in which the wavelength λ is either less or greater than 0.75μm. Water vapor absorbs in the near infrared region where $0.7\mu m \leq \lambda \leq 2.1\mu m$, ozone absorbs in the ultraviolet and visual region where $\lambda \leq 0.35\mu m$ and $0.5\mu m \leq \lambda \leq 0.7\mu m$. Carbon dioxide absorbs in the region which overlays with water vapor absorption where $2.1\mu m \leq \lambda \leq 2.9\mu m$. Therefore, the 0.75μm wavelength is an appropriate line of demarcation. Ozone absorption is dominant for $\lambda < 0.75\mu m$ while water vapor and carbon dioxide absorption are significant for $\lambda > 0.75\mu m$. This approach allows the partitioning of the specular variation of reflectance, transmittance and absorptance such that 51.7% is at wavelengths less than 0.75μm and 48.3% for $\lambda > 0.75\mu m$.

Following Stephens (1978), the parameterization of reflectance, transmittance and absorptance of a cloud layer is as follows:

(1) In the ultraviolet and visual region ($\lambda < 0.75\mu m$), the reflectance (Re_1), transmittance (Tr_1) and absorptance (A_1) are parameterized as

$$Re_1(\mu_0) = \frac{\beta_1(\mu_0)\tau_N/\mu_0}{1 + \beta_1(\mu_0)\tau_N/\mu_0} \tag{58}$$

$$Tr_1(\mu_0) = 1 - Re_1(\mu_0) \tag{59}$$

$$A_1(\mu_0) = 0. \tag{60}$$

(2) In the near infrared region ($\lambda > 0.75\mu m$), the reflectance (Re_2), transmittance (Tr_2) and absorptance (A_2) are evaluated as

$$Re_2(\mu_0) = (u^2 - 1)[\exp(\tau_{\text{eff}}) - \exp(\tau_{\text{eff}})]/R \tag{61}$$

$$Tr_2(\mu_0) = 4u/R \tag{62}$$

$$A_2(\mu_0) = 1 - Re_2(\mu_0) - Tr_2(\mu_0) \tag{63}$$

where

$$u^2 = [1 - \omega_0 + 2\beta_2\omega_0]/(1 - \omega_0) \tag{64}$$

$$\tau_{\text{eff}} = \{(1 - \omega_0)[1 - \omega_0 + 2\beta_2\omega_0)\}^{1/2}\, \tau_N/\mu_0 \tag{65}$$

$$R = (u + 1)^2 \exp(\tau_{\text{eff}}) - (u - 1)^2 \exp(-\tau_{\text{eff}}); \tag{66}$$

τ_N is the optical thickness of the cloud layer which is defined by

$$\log_{10}(\tau_{N_1}) = 0.2633 + 1.7095 \log_e [\log_{10}(W)] \tag{67}$$

when $\lambda < 0.75\mu$m. Also

$$\log_{10}(\tau_{N_2}) = 0.3492 + 1.6518 \log_e [\log_{10}(W)] \tag{68}$$

when $\lambda > 0.75\mu$m, where W is the liquid water path length (g m^{-2}) defined by

$$W = \int_0^{\Delta z} \rho_o r_l \, dz \tag{69}$$

where Δz is the thickness of the cloud layers. ω_0 is the single-scattering albedo, β_1 and β_2 are the back-scattered fraction of monodirectional incident radiation at zenith angle ϕ.

Coefficients ω_0, β_1, and β_2 are a function of τ_N and μ_0. Stephens (1978) developed a regression equation for ω_0, β_1, and β_2 from observational data. In this paper, a simple linear interpolation method is used to calculate those coefficients.

A brief summary of the above mentioned scheme is as follows:

(i) Two bands are considered. The wavelength for the line of demarcation is 0.75μm.

(ii) Absorption by cloud droplets in the ultraviolet and visual region ($\lambda < 0.75\mu$m) is ignored.

(iii) Absorption by cloud droplets only occurs in the near infrared region ($\lambda > 0.75\mu$m).

(iv) Reflectance, transmittance and absorptance are functions of the cloud optical thickness, droplet single-scattering albedo, backward scattering fraction and zenith angle.

Finally, the integrated reflectance, transmittance and absorptance of the cloud layer can be written as

$$Re = 0.517Re_1 + 0.483Re_2 \tag{70}$$

$$Tr = 0.517Tr_1 + 0.483Tr_2 \tag{71}$$

$$A = 0.483A_2. \tag{72}$$

4.4. PARAMETERIZATION OF REFLECTANCE, TRANSMITTANCE AND ABSORPTANCE OF A 'CLEAR-CLOUD MIXED' ATMOSPHERE

When the air column contains a cloud layer, the 'Yamamoto' type parameterization of absorptance for a clear atmosphere [Equation (53)] fails to function properly. Stephens (personal communication) overcame this shortcoming by assuming zero absorptance underneath the cloud layer. However, a new scheme is developed in this paper as follows:

The transmittance of a clear atmosphere can be defined by the summation of exponential functions (Stephens, 1977), as:

$$Tr(m) = \sum_{n=1}^{3} W_n \exp(-K_n m) \tag{73}$$

$$= \sum_{n=1}^{3} W_n \, Tr_n(m)$$

where $Tr_n(m) = \exp(-K_n m)$, m is the optical path length of water vapor, K_n is the equivalent extinction coefficient, and W_n is the weighting function. The coefficients W_n and K_n are derived from an experimental fit of the 'Yamamoto' absorption function and are given in Table II.

TABLE II

Values of the parameter in Equation (73)

n	1	2	3
W_n	0.12096	0.80556	0.07348
K_n	0.19649	0.00132	7.8179

Following this procedure, the entire solar spectrum can be imagined to be divided into three bands. In each band, the transmittance (Tr) can be represented by the exponential function. The advantage of this scheme is that the transmittance between the lth and $(l + 1)$th layer can be simply represented by

$$Tr_{n/l} = \exp(-K_n(m_{l+1} - m_l)) \tag{74}$$

where m_l (g cm^{-2}) is the total optical length of water vapor above the lth layer.

Yamamoto's absorptance [Equation (53)] can also be represented by

$$A(m) = 1 - Tr(m). \tag{75}$$

Because $Tr(m)$ is partitioned artificially into three bands, the absorptance in each band can then be written as

$$A_n(m) = 1 - Tr_n(m). \tag{76}$$

Thus, the 'actual' absorptance between the lth and $(l + 1)$th layer in each band can be expressed as

$$\begin{aligned} A_{n/l} &= A_n(m_{l+1}) - A_n(m_l) \\ &= (1 - \exp(-K_n m_{l+1})) - (1 - \exp(-K_n m_l)) \\ &= Tr_n(m_l)(1 - Tr_{n/l}) \end{aligned} \tag{77}$$

where $Tr_n(m_l)$ is the transmittance of the atmosphere above the lth layer. For a clear atmosphere, $Tr_n(m_l)$ can be expressed by

$$Tr_n(m_l) = \exp(-k_n m_l). \tag{78}$$

For the 'clear-cloud mixed' atmosphere, the expression is somewhat different,

$$Tr_n(m_l) = \prod_{i=1}^{l-1} Tr_{n/i}. \tag{79}$$

Equations (78) and (79) are identical if there is no cloud layer in the atmosphere. The total optical path length of the water vapor (m_l) can also be written as

$$m_l = \sum_{i=1}^{l-1} \rho_0 r_v (Z_{i+1} - Z_i). \tag{80}$$

Equation (79) can simulate the presence of a cloud layer. If the ith layer is a deck of cloud, the transmittance of the cloud layer can be calculated by Stephens' (1978) parameterization.

The following equations represent the procedure to compute radiative variables (A_n, Tr_n, and Re_n) in the clear-cloud mixed atmosphere.

$$Tr_{n/1} = H(0.517Tr_1 + 0.483Tr_2) + (1 - H)\exp(-K_n(m_{l+1} - m_l)) \tag{81}$$

$$A_{n/l} = 0.483HA_2 + A_{oz\,n/l} + (1 - H)Tr_n(m_l)(1 - Tr_{n/l}) \tag{82}$$

$$Re_{n/l} = H(0.517Re_1 + 0.483Re_2) + (1 - H)Re_{\text{clear}} \tag{83}$$

$$Tr_{n/l} = 1 - A_{n/l} - Re_{n/l} \tag{84}$$

$$Tr_n(m_{l+1}) = \prod_{i=1}^{l} Tr_{n/i} \tag{85}$$

where H is the cloud fractional coverage, and Equation (81) represents the first estimation of the transmittance. The radiative variables $Re_{n/l}$, $Tr_{n/l}$, and $A_{n/l}$ are the 'actual' reflectance, transmittance and absorptance between the lth and $l + 1$th layer. $Tr_n(m_{l+1})$ represents the total transmittance above the $l + 1$th layer.

5. Partial Condensation Scheme

Traditionally, various cloud models have been formulated such that the amount of cloud water is diagnosed by an 'all or nothing' scheme (see for example, Orville and Kopp, 1977; Klemp and Wilhelmson, 1978; Cotton and Tripoli, 1978). According to this scheme, condensation occurs only when the mixing ratio of the air, averaged over a horizontal domain, reaches the saturation mixing ratio determined from the average

temperature over the domain. As pointed out by Sommeria and Deardorff (1977), the sudden release of latent heat may produce a 'shock' to the model. Moreover, the entrainment of dry environmental air may dissipate parts of a cloud instead of the entire cloud layer as the 'all or nothing' scheme would predict. Also, it will be shown that in conjunction with the radiation model, the partial condensation scheme alters the evolution of the stratocumulus-capped mixed layer.

Several partial condensation schemes have been described in the literature. Sommeria and Deardorff (1977), Mellor (1977), and Bougeault (1981) assume that the joint probability density function for θ_l and r is distributed normally. Manton and Cotton (1977) and Banta and Cotton (1980), however, assume a normal distribution for $r - r_s$, where r and r_s are the total water mixing and saturation mixing ratio, respectively.

Although Mellor (1977) assumes a bi-normal distribution for θ_l and r, he re-derived the equation and obtained a new variable which is normally distributed. This new variable can be expressed as $ar'' - b\theta_l''$, where a and b are coefficients, r'' and θ_l'' are the fluctuation of total water mixing ratio and liquid water potential temperature. The positive fluctuation of r'' and the negative fluctuation of θ_l'' are associated with the positive fluctuation of r_c''.

The following scheme to represent partial condensation is adopted. The cloud water mixing ratio r_c can be expressed as

$$r_c = r - r_s(T) \tag{86}$$

where r is the total water mixing ratio and $r_s(T)$ is the saturation mixing ratio at temperature T. r and $r_s(T)$ can be decomposed into a mean quantity and turbulence fluctuation, i.e.,

$$r = \bar{r} + r'' \tag{87}$$

$$r_s(T) = r_s(\overline{T}) + r_s'' .$$

Therefore, r_c can be written as

$$\begin{aligned} r_c &= (\bar{r} - r_s(\overline{T}) + r'' - r_s'' \\ &= \bar{r}_{c0} + r_c'' . \end{aligned} \tag{88}$$

The amount of the condensed cloud water in the traditional 'all or nothing' is simply $\bar{r}_{c0} = \bar{r} - r_s(\overline{T})$. The fluctuation of cloud water is given by $r_c'' = r'' - r_s''$.

The turbulence fluctuation of saturation mixing ratio r_s'' can be derived as follows. From the equation of state,

$$e_s = R_v \rho_s T \tag{89}$$

where e_s is the saturation water vapor pressure, R_v is the specific gas constant for water vapor, and ρ_s is the saturation vapor density. The linearized form of (89) can be written as

$$\frac{e_s''}{e_{s0}} = \frac{\rho_s''}{\rho_{s0}} + \frac{T''}{T_0} \tag{90}$$

where the subscript '0' denotes a reference state. From the Clausius-Clapeyron equation, the following equation can be obtained

$$\frac{e_s''}{e_{s0}} = \frac{L_{lv}T''}{R_v T_0^2} \tag{91}$$

where L_{lv} is the latent heat of evaporation. Substituting Equation (91) into Equation (90), we obtain

$$\frac{\rho_s''}{\rho_{s0}} = \left(\frac{L_{lv}}{R_v T_0} - 1\right)\frac{T''}{T_0} = \left(\frac{L_{lv}}{R_v T_0} - 1\right)\frac{\theta''}{\theta_0}. \tag{92}$$

The turbulent fluctuation of the saturation mixing ratio r_s'' can be defined as

$$r_s'' = \frac{\rho_s''}{\rho_d} \tag{93}$$

where ρ_d is the dry air density. Equation (92) then becomes

$$r_s'' = r_{s0}\left(\frac{L_{lv}}{R_v T_0} - 1\right)\frac{\theta''}{\theta_0} \tag{94}$$

where $r_{s0} = \rho_{s0}/\rho_d$. Fluctuations in θ_{il} can be written as

$$\frac{\theta_{il}''}{\theta_{il0}} = \frac{\theta'}{\theta_0} - \frac{L_{lv}}{c_{pa}T_0}(r_c'' + r_R'' + r_i'') \tag{95}$$

where r_R'' and r_i'' are fluctuations of rain water and cloud ice mixing ratio. Substitution of Equation (95) into Equation (94) allows us to represent r_s'' as

$$r_s'' = r_{s0}\left(\frac{L_{lv}}{R_v T_0} - 1\right)\left(\frac{\theta_{il}''}{\theta_{il0}} + \frac{L_{lv}}{c_{pa}T_0}(r_c'' + r_R'' + r_i'')\right). \tag{96}$$

In this paper, rain and ice are not included; thus $r_R'' = 0$, $r_i'' = 0$.

As shown in Equation (88), the turbulence fluctuation of cloud water mixing ratio is defined by

$$r_c'' = r'' - r_s''. \tag{97}$$

Substitution of Equation (96) into Equation (97) and rearranging allows us to rewrite r_c'' as

$$r_c'' = a_2(r'' - \alpha_2\theta_{il}'') \tag{98}$$

where

$$a_2 = \left[1 + \frac{L_{lv}r_s(T_0)}{c_{pa}T_0}\left(\frac{L_{lv}}{R_v T_0} - 1\right)\right]^{-1}$$

$$\alpha_2 = r_s(T_0)\left(\frac{L_{lv}}{R_v T_0} - 1\right)/\theta_{il0}.$$

The normalized form of Equation (98) can be written as

$$t = \frac{r_c''}{\sigma_c} = \frac{a_2}{\sigma_c}(r'' - \alpha_2 \theta_{il}'') \tag{99}$$

where σ_c is the standard deviation of r_c'', and can be defined by

$$\sigma_c = [a_2^2(\overline{r''^2} + \alpha_2^2 \overline{\theta_{il}''^2} - 2\alpha_2 \overline{\theta_{il}'' r''})]^{1/2}. \tag{100}$$

In Equation (99), t is the normalized variable which is assumed to be distributed according to a probability density function (G).

The following equations represent the scheme to diagnose the cloud fractional coverage (H), mean cloud water mixing ratio ($\bar{r}_c$) and cloud water variance ($\overline{r_c''^2}$):

$$H = \int_{-Q_1}^{\infty} G(t)\,\mathrm{d}t \tag{101}$$

$$\bar{r}_c/\sigma_c = \int_{-Q_1}^{\infty} (Q_1 + t)\, G(t)\,\mathrm{d}t \tag{102}$$

$$\overline{r_c''^2}/\sigma_c = \int_{-Q_1}^{\infty} (Q_1 + t)t\, G(t)\,\mathrm{d}t \tag{103}$$

where $Q_1 = \bar{r}_{c0}/\sigma_c$, $G(t)$ is the probability density function.

Usually the probability density function G is normally distributed. However, some simplifications of this probability density function have been tested by Banta and Cotton (1980) and Bougeault (1981). In this paper, two types of probability density function are adopted and tested. Figure 2 is a schematic representation of those two functions. Table III represents the parameterization of cloud fractional coverage (H), mean cloud water mixing ratio ($\bar{r}_c$) and cloud water variance ($\overline{r_c''^2}$) for the uniformly distributed probability density function and the positively-skewed distribution function.

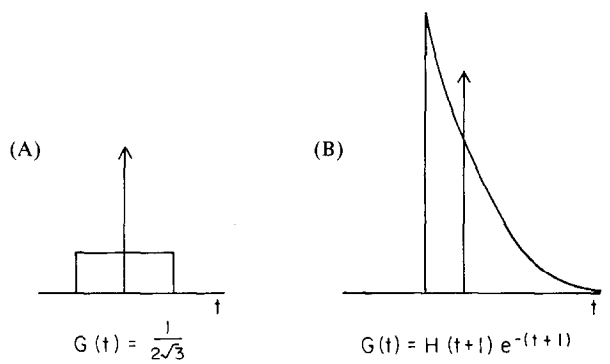

Fig. 2. Schematic representation of the probability density function (PDF). (A): Uniformly distributed PDF (B): Skewed PDF.

TABLE III

Parameterizations of H, $\bar{r}_c/\sigma_c$ and $\overline{r''^2}/\sigma_c^2$

$G(t)$	$\frac{1}{2\sqrt{3}}$		$h(t+1)e^{-(t+1)}$	
H	0;	$Q_1 \le -\sqrt{3}$	e^{Q_1-1};	$Q_1 \le 1$
	$(Q_1+\sqrt{3})/2\sqrt{3}$;	$-\sqrt{3} < Q_1 < \sqrt{3}$	1;	$Q_1 \ge 1$
	1;	$Q_1 \ge \sqrt{3}$		
$\bar{r}_c/\sigma_c$	0;	$Q_1 \le \sqrt{3}$	e^{Q_1-1};	$Q_1 \le 1$
	$\sqrt{3}H^2$;	$-\sqrt{3} < Q_1 < \sqrt{3}$	Q_1;	$Q_1 \ge 1$
	Q_1;	$Q_1 \ge \sqrt{3}$		
$\overline{r_c''^2}/\sigma_c^2$	0;	$Q_1 \le -\sqrt{3}$	$(2-Q_1)e^{Q_1-1}$;	$Q_1 \le 1$
	$\left(\sqrt{3}+\frac{Q_1^3}{3}\right)/2\sqrt{3}$;	$-\sqrt{3} < Q_1 < \sqrt{3}$	1;	$Q_1 \ge 1$
	1;	$Q_1 \ge \sqrt{3}$		

Finally, the second-order and third-order cloud water correlations are approximated as:

$$\overline{\alpha'' r_c''} = (a_2 \overline{\alpha'' r''} - b_2 \overline{\alpha'' \theta_{il}''})H \tag{104}$$

$$\overline{\alpha'' \beta'' r_c''} = (a_2 \overline{\alpha'' \beta'' r''} - b_2 \overline{\alpha'' \beta'' \theta_{il}''})H \tag{105}$$

where α'' and β'' are any turbulent variable, and

$$b_2 = a_2 \alpha_2 .$$

6. Initial Conditions and Description of Experiments

The initial conditions are derived from the numerical results at the end of Wangara Day 33 experiment (Chen and Cotton, 1983). Since this is a dry case, no cloud formation can be expected. In order to initiate a stratocumulus layer, the boundary layer is cooled by 3° K and warmed by 3.75° K above the boundary layer. This produces a sharp inversion across the top of the boundary layer. In addition, 2.5 g kg^{-1} of moisture are added within the boundary layer and 1.6 g kg^{-1} of moisture are added above the boundary layer. A steady surface heat flux is maintained at 8.8×10^{-2} K m s^{-1}. The surface moisture flux is also maintained at 1.0×10^{-2} g kg^{-1} m s^{-1}. No large-scale subsidence is imposed. In keeping with our long-range goal of adapting this turbulence model to a 'sophisticated' mesoscale model with horizontal resolution between 5 and 20 km, we have selected a vertical grid interval of 100 m. Using stretched vertical coordinates, such vertical resolution can be achieved in a mesoscale model run on a class 6 type computer. Finer vertical resolution than this would be impractical for use in such a model. The initial conditions described above are very similar to Deardorff's (1980b) simulation of a stratocumuli-capped mixed layer. However, Deardorff's simulation of the Wangara data had a deeper mixed layer; thus the initial height of the mixed layer in the following experiments is not as deep as Deardorff's.

TABLE IV

Design of the 5 numerical experiments

Exp.	L.W. radiation activated	S.W. radiation activated	PDF
1	No	No	uniform
2	Yes	No	"
3	Yes	Yes	"
4[a]	No	No	"
5[b]	Yes	No	skewed

[a] Rapid entrainment experiment.
[b] Results not shown.

Table IV shows the design of the five case studies. Experiment 1 represents the case without long-wave (L.W.) and short-wave (S.W.) radiation. This experiment is compared with Deardorff's (1980b) case 4 study. Experiment 2 is a case with only L.W. radiation activated, while experiment 3 has both L.W. and S.W. radiation activated.

Experiment 4 represents a simulation of rapid entrainment as discussed by Deardorff (1980a) and Randall (1980). In experiments (1–4), the uniformly distributed probability density function (PDF) is used. Experiment 5 is like experiment 2 except that the PDF is skewed as discussed by Bougeault (1981).

7. Results

7.1. Experiment 1 – no atmospheric radiation processes

Figure 3 illustrated the profiles of $\overline{\theta_{il}}$, $\overline{\theta_v}$, $\overline{w''\theta_{il}''}$, $\overline{w''\theta_v''}$, H, $\overline{r_c}$, $\overline{r}$, $\overline{w''r''}$, $\overline{w''r_c''}$ for experiment 1 at the end of the 30 min simulation time. The predicted height of the mixed

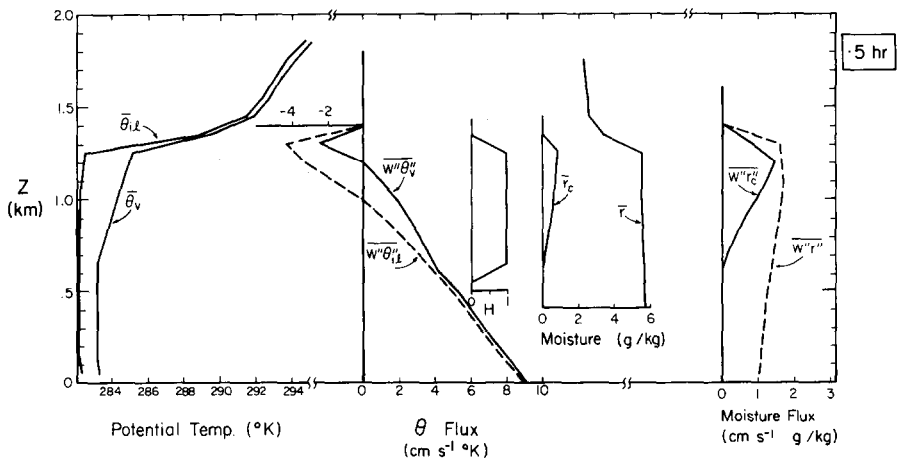

Fig. 3. Vertical profiles of mean ice-liquid water potential temperature ($\overline{\theta_{il}}$) and its vertical flux, vertical potential temperature ($\overline{\theta_v}$) and its vertical flux, cloud fractional coverage (H), total water mixing ratio ($\overline{r}$) and its vertical flux, cloud water mixing ratio $\overline{r_c}$ and its vertical flux. This result is at t = 30 min, for the case without L.W. and S.W. radiation.

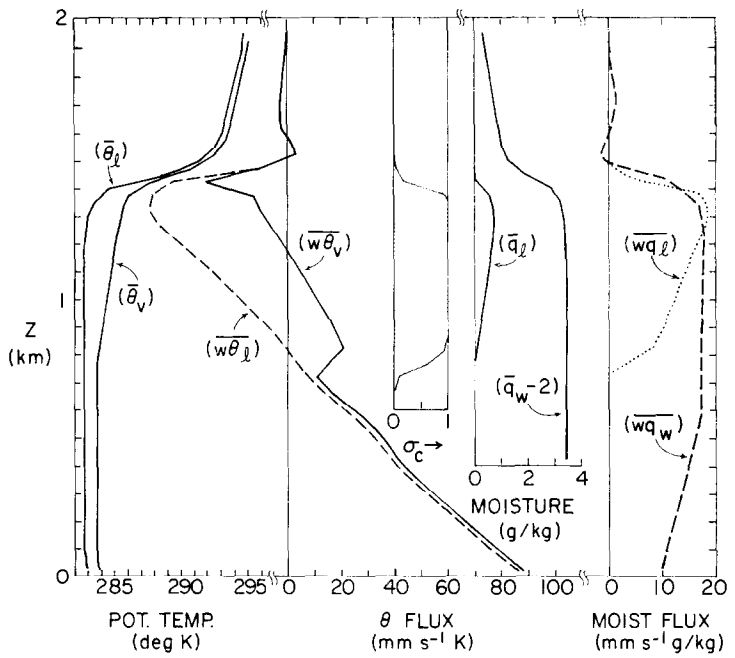

Fig. 4. From Deardorff (1980b). Vertical profiles of mean liquid-water potential temperature (θ_e) and its vertical flux, vertical potential temperature and its vertical flux, cloud fraction (σ_c) at a given height (stippled area), total specific moisture (q_w) and its vertical flux, and liquid-water specific humidity (q_l) and its vertical flux for the case without L.W. and S.W. radiation.

layer is 1300 m while Deardorff's model predicted a height of 1400 m (Figure 4). The difference is due to the initial condition as mentioned before. No significant residual tails for $\overline{w''\theta_{il}''}$, $\overline{w''r''}$ can be found above the mixed layer. In general, however, the results shown in Figure 3 are in good agreement with Deardorff's (Figure 4). As in Deardorff's simulation, the vertical heat flux $\overline{w''\theta_{il}''}$ is a linear function with respect to height. The buoyancy heat flux $\overline{w''\theta_v''}$ has a slight jump near the cloud base, which is due to the release of latent heat by condensation. As shown in Figure 4, this jump of $\overline{w''\theta_v''}$ is not as great as that obtained by Deardorff. The weaker jump in buoyancy flux in our case corresponds to an underestimation of $\overline{w''r_c''}$ near the cloud base. The predicted magnitude of the negative $\overline{w''\theta_{il}''}$ near the top of the mixed layer is about 50% of the surface heat flux while it is about 55% in Deardorff's case. The small difference between our result and Deardorff's could be attributed to the differences in initial conditions. By contrast, the predicted negative $\overline{w''\theta_{il}''}$ in the Wangara dry case (Chen and Cotton, 1983) was only 5% ~ 14% of the surface heat flux. Thus, the larger magnitude entrainment rate in the stratocumulus layer is a consequence of a positive feedback mechanism due to cloud top evaporational cooling. That is, the entrained dry air evaporates cloud water and intensifies the vertical mixing near the cloud top. As a result, the buoyancy heat flux $\overline{w''\theta_v''}$ does not have as large a negative value as $\overline{w''\theta_{il}''}$.

The vertical profile of cloud fraction shows that the whole cloud layer is quite solid (100% coverage). In Figure 4, Deardorff's case exhibits 'broken' cloud (less than 100%

coverage) near cloud top and cloud base. Based on the difference in the cloud fractional coverage profile, we suspect that the uniformly distributed probability density function may not be adequate for use in a stratocumulus cloud layer. The predicted cloud water mixing ratio $\overline{r_c}$ exhibits a steady increase from cloud base to cloud top and has a peak magnitude around 0.86 g kg^{-1}, which is similar to Deardorff's result.

The vertical total water flux $\overline{w''r''}$ exhibits a positive value within the entire mixed layer, which indicates the vertical mixing is 'moist up, dry down'. Since the vertical cloud water flux $\overline{w''r_c''}$ is parameterized as a function of $\overline{w''r''}$ and $\overline{w''\theta_{il}''}$, $\overline{w''r_c''}$ should have the same order magnitude as $\overline{w''r''}$. As mentioned before, this $\overline{w''r_c''}$ profile indicates some underestimation near the cloud base when it is compared with Deardorff's case (Figure 4). This underestimation can be traced back to the less intense $\overline{w''r''}$ near the cloud base. The positive value of $\overline{w''r_c''}$ can be interpreted as 'up condensation, down evaporation'. Both processes can increase the buoyancy heat flux.

7.2. Experiment 2 – The Case with L.W. Radiation

The result of introducing L.W. radiative cooling is shown in Figure 5. The main effect is to produce radiation cooling at the cloud top and relatively small warming at cloud base. The magnitude of the maximum cooling and warming are -97 K day^{-1} and 12° K day^{-1}, respectively. Brost *et al.* (1982) indicate that the L.W. radiation cooling is found within the uppermost 50 m of the cloud. Our use of a 100 m vertical grid spacing spreads the cooling effect over a somewhat deeper layer near cloud top.

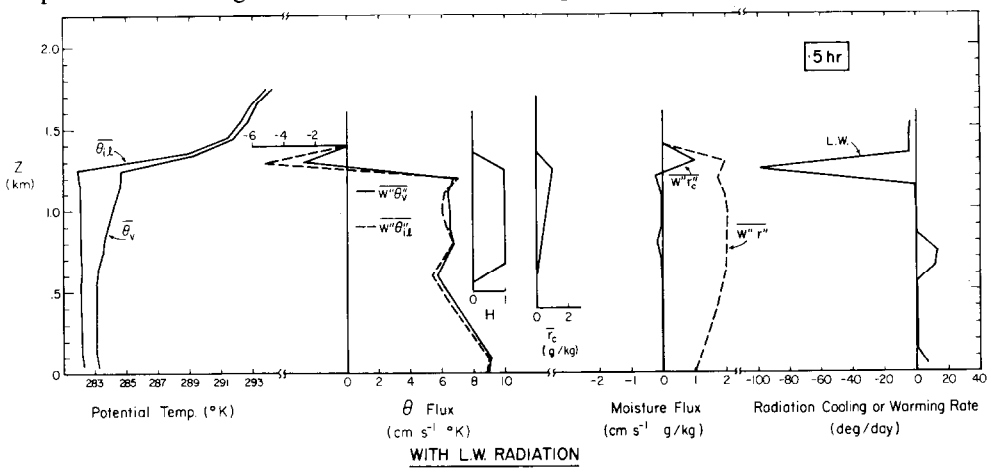

Fig. 5. As in Figure 3 except for the case with L.W. radiation. Vertical profile of the L.W. radiation cooling or warming rate is also shown.

In this simulation, the cooling occurs entirely within the upper mixed layer (where $H = 100\%$) which doesn't agree with Lilly's (1968) hypothesis that the radiation cooling is entirely within the capping inversion. The definition of the capping inversion is rather ambiguous in the literature. However, Deardorff (1980b) indicated that the capping inversion is the layer between the uppermost cloud-top domes and the lowermost cloud-top cusps. The cloud fraction within this layer varied with height between 100%

and 0%. According to Deardorff's definition for the capping inversion, Figure 5 illustrates that L.W. cooling doesn't occur within the capping inversion and the thickness of the capping inversion is negligible. During the transition period however, the cloud layer propagates upward another grid point. The diagnosed cloud fraction at the uppermost grid when the cloud is present is less than 100%. We can thus imagine that some cloud elements penetrate into the capping inversion. The thickness of the modelled capping inversion is only one grid interval (100 m). This results in some radiation cooling within the capping inversion. We will discuss this subject more fully later in this paper.

As a consequence of radiative cooling at the cloud top and radiative warming at the cloud base, the entire cloud layer becomes slightly unstable. Both $\overline{w'' \theta_{il}''}$ and $\overline{w'' \theta_v''}$ exhibit sharp departures from linearity just above cloud base in the L.W. radiation case. The field study of nocturnal stratocumulus reported by Caughey *et al.* (1982) indicates that large positive heat flux can be found near the cloud top. The destabilization of the cloud layer near the cloud top is the cause of the large positive heat flux.

In contrast to Figure 3, the entrainment rate (i.e., the negative heat flux $\overline{w'' \theta_{il}''}$) is increased only slightly from 50% to 58% of the surface heat flux in the L.W. radiation case. This is a consequence of our assumption that the surface heat flux is constant over the ocean throughout the integration. Thus when L.W. radiation cooling destabilizes the cloud top and initiates entrainment, the entrainment cannot be maintained continuously without the supply of kinetic energy from beneath the cloud top. However, since the surface heat flux is fixed, the additional energy cannot be obtained from the ocean surface. Instead, the kinetic energy needed to support entrainment must be produced within the convectively unstable cloud layer. Since radiation cooling causes only a slight destabilization of the entire cloud layer, the kinetic energy gain is relatively small, leading to only a slight enhancement of the rate of cloud-top entrainment.

The mean ice-liquid water potential temperature $\bar{\theta}_{il}$ shows a 'dip' near the cloud top (Figure 5). The results presented by Brost *et al.* (1982) and Deardorff (1980b) do not indicate any convective unstable layer near the cloud top. Thus, in the real world, this 'dip' may not exist. However, as will be discussed later, this feature is consistent with the physics of the model.

The mean cloud water profile $\bar{r}_c$ is altered only slightly by L.W. radiative transfer. Figure 5 indicates that L.W. radiative cooling at cloud top produces a slightly larger amount of $\bar{r}_c$ (0.12 gm kg^{-1}) near the cloud top. The $\overline{w'' r''}$ profile shows 10 to 15% more dry air entrained into the mixed layer compared with experiment 1 (Figure 3). In comparison with Deardorff's (1980b) result, the negative $\overline{w'' r_c''}$ does not seem realistic. However, the negative $\overline{w'' r_c''}$ is a result of the much larger $\overline{w'' \theta_{il}''}$ within the lower 2/3 of the cloud layer, i.e., positive fluctuations of θ_{il} tend to produce negative fluctuations of r_c.

7.3. Experiment 3 – the case with both L.W. and S.W. radiation

In this experiment, both the L.W. radiation model and the S.W. radiation model are activated. Throughout the entire simulation time, there is no time variation of solar zenith angle (ϕ), such that $\cos \phi = 0.7$.

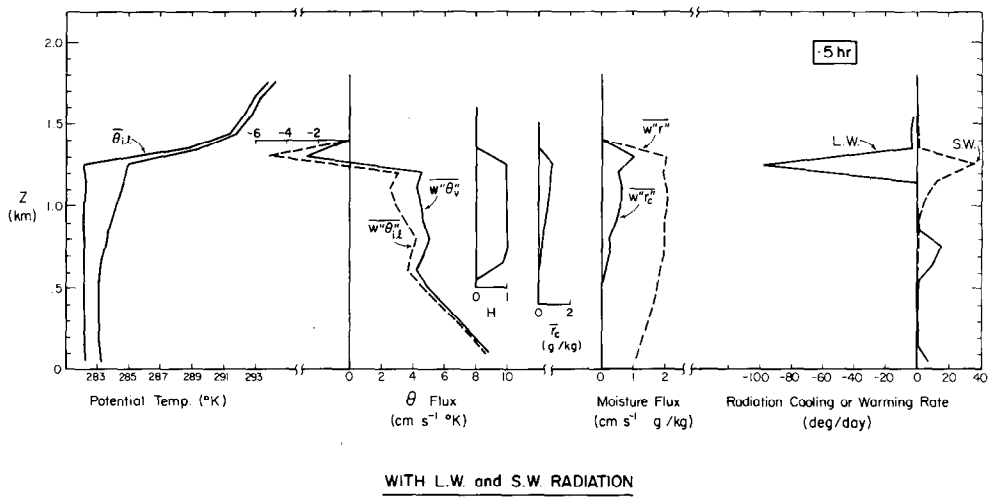

WITH L.W. and S.W. RADIATION

Fig. 6. As in Figure 3, except for the case with L.W. and S.W. radiation. Vertical profiles of the L.W. and S.W. radiation cooling or warming rate are also shown.

We are interested in comparing the short-wave radiation models of Oliver *et al.* (1978, hereafter referred to as OLW) and Stephens (1978). The absorption coefficient α^s for OLW is 16 cm^2 g^{-1}, while the interpreted α^s for the Stephens case is about 75 cm^2 g^{-1}. For a cloud with 1.0 g kg^{-1} cloud water content, the short-wave penetration distance estimated by OLW is 500 m, while for Stephens' case it is 111 m. The vertical profile of short-wave radiation warming rate shown in Figure 6 indicates that the major warming occurs at the upper 100 m (1 grid point). This is consistent with the analysis of the penetration distance. As shown in Figure 6, the cloud top L.W. radiation cooling is thus partially compensated by the S.W. radiation warming. The $\overline{\theta_{il}}$ profile shows that the cloud layer is somewhat less unstable than in experiment 2. As a consequence, the vertical heat flux inside the cloud layer is smaller than that in experiment 2. The magnitude of negative heat flux at the cloud top is almost the same as in experiment 2. The small difference in the negative heat flux at the cloud top among the three experiments (1, 2, 3) suggests that cloud-top entrainment rate is principally controlled by the surface heat flux. Because of the less intense heat flux inside the cloud layer, $\overline{w''r_c''}$ is positive and increases in magnitude from cloud base to cloud top.

Using Stephen's short-wave radiation parameterization, we find that there is little diurnal variation in the simulated cloud layer. This is a result of the fact that long-wave radiation cooling and short-wave radiation warming both take place in a relatively short distance from cloud top. Because of the strong L.W. cooling near the cloud top, S.W. heating is not able to dissipate the cloud. Large-scale subsidence is considered to be the most important contributing factor to the diurnal variation of stratocumulus in coastal regions. The current sensitivity experiments, however, do not include this factor.

OLW found that the diurnal variation of the cloud layer is significant in their sensitivity experiments. They claimed that clouds are evaporated away by turbulent transfer of solar energy captured in the cloud interior. This is a consequence of the small

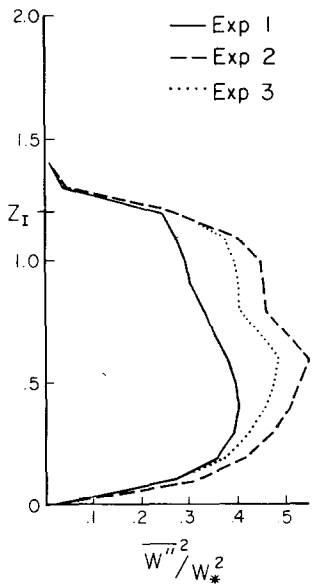

Fig. 7. Vertical profiles of the normalized vertical velocity variance, at t = 30 min. Solid line represents the case without radiation, while the dotted line represents the case with both L.W. and S.W. radiation model activated. Dashed line is the case with L.W. radiation model activated.

absorption coefficient α^s they employed. As a result, the S.W. radiation can penetrate deeper into the cloud layer.

7.4. A COMPARISON OF EXP. 1, EXP. 2, AND EXP. 3

Figure 7 shows the normalized variance of vertical velocity ($\overline{w''^2}/w^{*2}$) for the three experiments, where w^* is the surface convective velocity. It is defined by $w^* = (g\,\overline{w''\theta_{il}''}\,Z_I/\bar{\theta}_{il})_s^{1/3}$. Z_I is the height of the inversion, s denotes surface. The profile of $\overline{w''^2}$ is consistently smaller in magnitude in Exp. 1. Moreover, the maximum of $\overline{w''^2}$ is located below the cloud base where $Z/Z_I \simeq 0.3$. This maxima is associated with the surface heat flux. In the companion paper (Chen and Cotton, 1983), our Wangara numerical experiments show that the mid-convective boundary layer has a maximum of $\overline{w''^2}$ near $Z/L_I = 0.25 \sim 0.3$. Here, the largest magnitude of $\overline{w''^2}$ occurred in Exp. 2. Both Exp. 2 and Exp. 3 have a maximum of $\overline{w''^2}$ near the cloud base. There is a slight appearance of a near-secondary maximum at 1.0 km for all three experiments. This is consistent with Deardorff's (1980b) 3D simulation of the stratocumulus-capped mixed layer where he found a strong secondary maximum of $\overline{w''^2}$ near the cloud top. He claimed that the secondary maximum is caused by the entrainment-induced evaporative cooling. The lesser intensity of the secondary maximum in our experiments, however, may indicate that evaporation cooling is not as large as in Deardorff's simulation.

The budget analysis of the heating rate for all three experiments is shown in Figures 8, 9, and 10. In the left panel of the figures, the heating rate due to sensible heat for the entire boundary layer is calculated by $\overline{w''\theta_{il}''}/(Z_I - Z_0)$. The heating rate for the cloud layer only, is calculated by $\overline{w''\theta_{il}''}/(Z_I - Z_B)$. This explains why SH into cloud top has

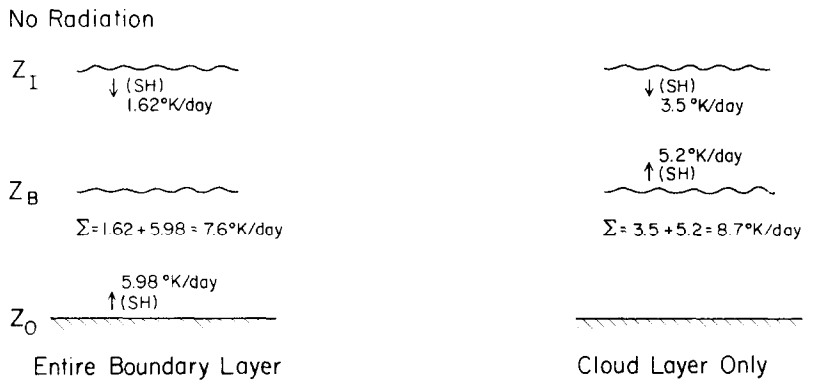

Fig. 8. The budget analysis of the heating rate for the case without radiation. SH denotes the heating rate due to the sensible heat. Σ represents the summation of various heat sources. The left panel is the analysis for the entire boundary layer, while the right panel is only for the cloud layer.

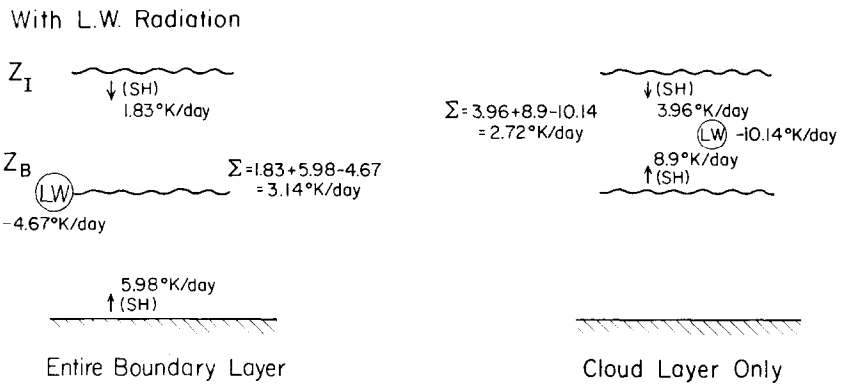

Fig. 9. As in Figure 8, except for the case with L.W. radiation.

different values. Exp. 1 exhibits the largest net heating rate, while Exp. 2 produces the smallest. The entrainment-induced sensible heating rate differs little among the three experiments. Thus, the cloud top L.W. radiation cooling does not significantly intensify the entrainment rate. It is thus obvious that entrained warmer air cannot balance the cloud top radiation cooling. As shown in Figure 9, the largest sensible heating rate imported from the cloud base occurs in Exp. 2. This suggests that the vertical heat flux is modulated by radiation cooling and warming. Thus, the cloud-top radiation cooling is balanced by the enhanced eddy heat flux from cloud base. Brost *et al.* (1982) infer in their case study that the cloud top radiation cooling is balanced by the entrainment of warm air. In their case, however, strong wind shear across the cloud top may have been a contributing factor to their different conclusion.

7.5. Further analysis of experiment 2

Figure 11 represents the simulation of Exp. 2 at time 2.5 hr. The main feature is that the cloud water starts to appear at a height of 1400 m (one grid upward) where the cloud

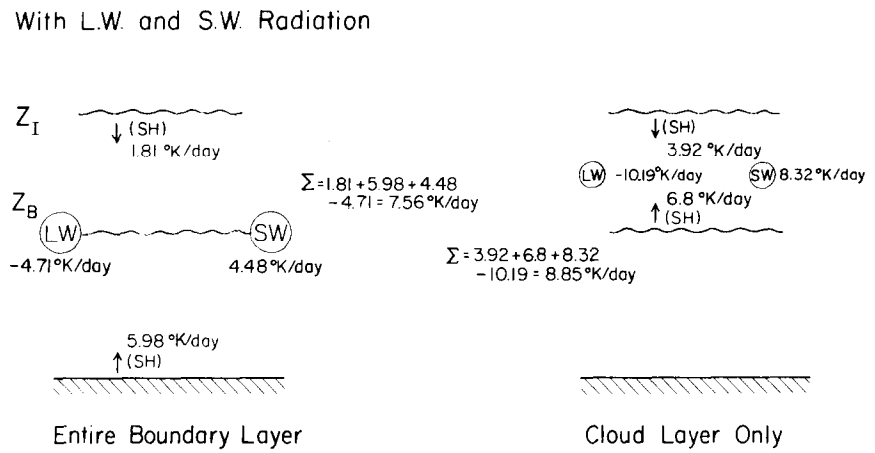

Fig. 10. As in Figure 8, except for the case with L.W. and S.W. radiation.

fraction is less than 100%. As mentioned before, during the steady period of the cloud, L.W. radiation cooling is entirely within the upper mixed layer. However, during this transient period, most of the radiation cooling is within the capping inversion. This is consistent with Lilly's assumption in his mixed-layer model.

In Figure 11, a relatively large negative $\overline{w''\theta_{il}''}$ and positive $\overline{w''r''}$ can be found at the top of the mixed layer. This indicates the presence of vigorous entrainment at the top of the mixed layer. Because radiation cooling is within the capping inversion, the temperature at the capping inversion falls rapidly. Thus the requirement for cloud-top entrainment instability that $\Delta\theta_e = -1$ to -3° K is satisfied (Deardorff, 1980a; Randall, 1980). This enhanced entrainment is actually a special case of the occurrence of 'rapid' entrainment.

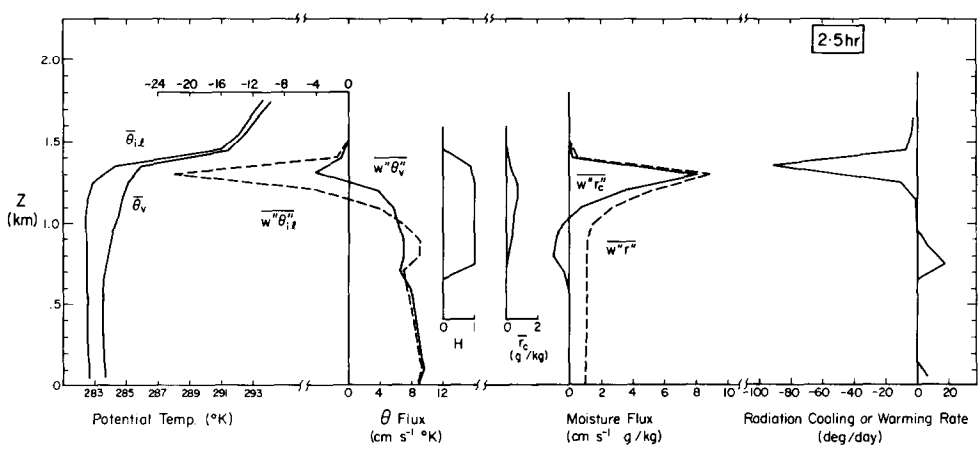

Fig. 11. As in Figure 9, except at t = 2.5 hr.

As discussed before, the cloud-top radiation cooling can not be balanced by the entrainment of warm air. The only mechanism to remove this cooling is the enhanced vertical heat flux from the cloud base. The vertical heat flux always acts to decrease the local instability near cloud top. However, it does not always respond fast enough to destroy the local instability. Therefore, the 'dip' of $\bar{\theta}_{il}$ at the cloud top noted in Section 7.2 is physically reasonable for this model. This result does not agree with Brost *et al.* (1982) and Deardorff (1980b), however. A likely source of this discrepancy is the scheme to predict the cloud fractional coverage near the cloud top. The diagnosed cloud fractional coverage at the cloud top in experiment 2 is 100%. Deardorff (1980b) applied radiation cooling at the uppermost grid volume in each vertical column for which mean cloud water exceeded 0.01 gm kg^{-1}. His figure 7 shows that the radiative cooling occurs within the mean capping inversion (which includes cloud-top domes) and the upper part of the cloud layer where the cloud fractional coverage is less than 100%. Thus, .a better scheme to diagnose the cloud fractional coverage at the cloud top is needed.

Bougeault's (1981) positively skewed probability density function is also tested. The results, similar to Figure 3, indicated that the prediction of cloud fractional coverage at the cloud top is not altered very much. The selection of the appropriate probability density function for cloud cover certainly requires further investigation. Both observational studies and large-eddy explicit cloud simulations are needed.

7.6. The rapid entrainment experiment

In order to initiate rapid entrainment, cooling is applied between 1300 and 1200 m. Similar to Deardorff (1980b) the magnitude of the cooling is about 10° K and can be seen in the $\bar{\theta}_{il}$ profile shown in Figure 12. The slight warming within the mixed layer is due to surface heating and warming by the entrained air. A very significant negative $\overline{w''\theta_{il}''}$ and positive $\overline{w''r_c''}$ indicate that evaporation of descending air is a dominant feature in the upper part of the cloud layer. Because of the larger evaporative cooling, the buoyancy flux $\overline{w''\theta_v''}$ no longer has a negative peak near the top of the mixed layer as seen in experiments 1, 2, and 3. Compared to Deardorff (1980b, case 5), some similarity can be found. However, the magnitude of the entrainment for this experiment is larger than that of Deardorff's. The reason may be due to more cooling applied above the boundary layer. The orders of magnitude of $\overline{w''\theta_{il}''}$, $\overline{w''\theta_v''}$, $\overline{w''r''}$, and $\overline{w''r_c''}$ between this experiment and Deardorff's case are very close.

The cloud fraction profile shows that the cloud grows much higher following the cooling of the upper layer. The entire cloud layer is not a solid deck, however, since regions of cloud fraction less than one are evident inside the cloud layer. Both the $\bar{r}_c$ and H profiles show fluctuations with height. These fluctuations can be traced back to the $\overline{\theta_{il}}$ profile which also exhibits the same pattern. These fluctuations are probably a consequence of the nonlinear coupling among the processes of entrainment and cloud fraction.

The profile of $\overline{w''^2}$ also exhibits a dramatic change. The magnitude of $\overline{w''^2}$ is much larger in the rapid entrainment experiment than in the previous experiments. Moreover, the maximum $\overline{w''^2}$ is elevated to well within the cloud layer. This higher level of $\overline{w''^2}$ is

due to the large amount of evaporational cooling or buoyant production of turbulence. Deardorff's case 5 (his Figure 9) shows that the maxima $\overline{w''^2}$ is located near the cloud top, which is due to the cloud-top evaporative cooling. The maxima of $\overline{w''^2}$ in our case is within the cloud layer. It seems to us that in Figure 12, the cloud-top evaporative cooling extends far down into the cloud.

8. Concluding Remarks

The following conclusions can be drawn from this study:

(i) The small difference in the rate of entrainment among experiments 1, 2, and 3 indicates that for these cases, surface heating is the primary mechanism controlling the rate of entrainment.

(ii) Cloud-top radiative cooling is not balanced by the entrainment of warmer air. Instead it is mostly compensated by enhanced heat flux from cloud base.

(iii) Due to the vertical distribution of radiation warming and cooling, $\overline{w''\theta_{il}''}$ is highly nonlinear within the cloud layer.

(iv) During the transient period, the capping inversion is cooled very rapidly by radiative cooling.

(v) Consistent with the findings of Deardorff (1980a) and Randall (1980), rapid entrainment occurs when the $\bar{\theta}_e$ jump at the cloud top is between -1 to $-3°$ K.

(vi) The experiments with L.W. radiation cooling exhibit larger $\overline{w''^2}$ and the maxima of $\overline{w''^2}$ is then located near the cloud base.

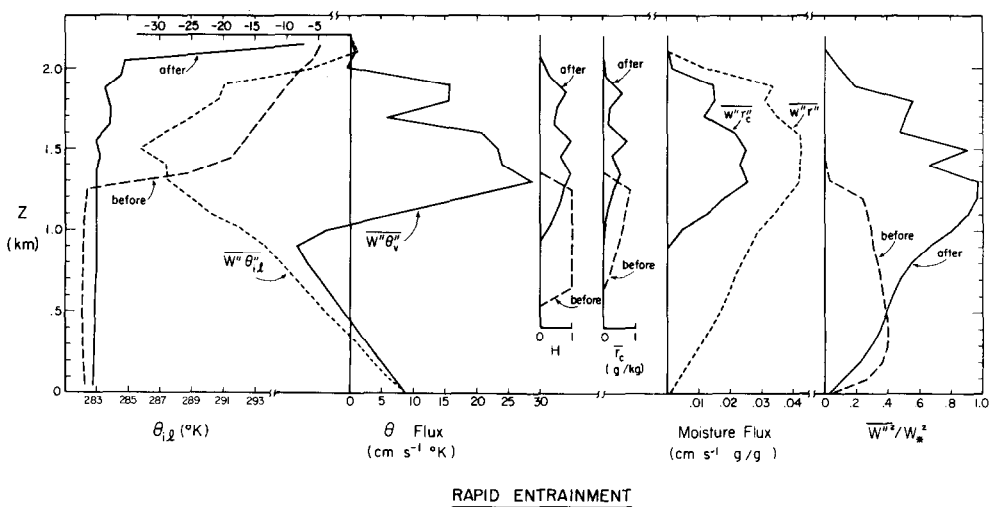

Fig. 12. Vertical profiles of mean ice-liquid water potential temperature ($\bar{\theta}_{il}$) and its vertical flux, vertical flux of vertical potential temperature ($\overline{w''\theta_{il}''}$, $\overline{w''\theta_v''}$), cloud fractional coverage (H), mean cloud water mixing ratio ($\bar{r}_c$) and its vertical flux, vertical flux of total water mixing ratio, and the normalized vertical velocity variance. The dashed lines represent the case before the onset of rapid entrainment, solid lines represent the case after the onset of rapid entrainment.

(vii) The selection of the probability density function may be very important for the prediction of cloud fractional coverage near the cloud top.

(viii) The evolution of the cloud layer after the initiation of rapid entrainment involves a complicated nonlinear coupling among entrainment, cloud fraction and radiative cooling.

Overall, the model appears to be a very general model of the transient behavior of stratocumulus cloud layers. The parameterization of the turbulence time scale introduced here for the unstable layer inside the cloud seems to function reasonably. This one-dimensional model has been able to reproduce a number of features predicted by Deardorff's three-dimensional model at a reduction of computational cost of approximately two orders of magnitude. We recommend that both modelling approaches (i.e., Deardorff's large-eddy simulations and higher-order 1D models) be tested against actual observations of stratocumulus layers.

Acknowledgements

The authors wish to thank Mr Gregory J. Tripoli for his help in the modeling. Dr Robert Banta is also acknowledged for his suggestions and discussion. Special thanks are due to Dr Graeme Stephens for his instructions in setting up the radiation model. We also wish to thank Dr D. H. Lenschow and R. A. Brost for their helpful discussion and advice. Our special gratitude extends to Ms. Brenda Thompson for typing this difficult manuscript and Ms. Judy Sorbie for her work in drafting the figures. This work was supported under Office of Naval Rresearch (ONR) Contract # N00014–79–C–0793, and under National Science Foundation Grant # ATM–7908297. Computations were performed on the National Center for Atmospheric Research (NCAR) CRAY I computer. NCAR is supported by the National Science Foundation.

References

André, J. C., DeMoor, C., Lacarrere, P., Therry, G., and DuVachat, R.: 1978, 'Modeling thr 24-hr Evolution of the Mean and Turbulent Structures of the Planetary Boundary Layer', *J. Atmos. Sci.* **35**, 1861–1883.

Banta, R. and Cotton, W. R.: 1980, 'On Computing Average Cloud-Water Quantities in a Partially-cloudy Region', *J. de Rech. Atmos.* **14**, 487–492.

Blackadar, A. K.: 1962, 'The Vertical Distribution of Wind and Turbulent Exchange in Neutral Atmosphere', *J. Geophys. Res.* **67**, 3095–3102.

Bougeault, Ph.: 1981, 'Modeling the Trade-wind Cumulus Boundary Layer. Part I: Testing the Ensemble Cloud Relations Against Numerical Data', *J. Atmos. Sci.* **38**, 2414–2424.

Brost, R. A., Wyngaard, J. C., and Lenschow, D. H.: 1982, 'Marine Stratocumulus Layers. Part II: Turbulence Budgets', *J. Atmos. Sci.* **39**, 818–836.

Caughey, S. J., Crease, B. A., and Roach, W. T.: 1982, 'A Field Study of Nocturnal Stratocumulus. Part II: Turbulence Structure and Entrainment', *Quart. J. Roy. Meteorol. Soc.* **108**, 125–144.

Chen, C. and Cotton, W. R.: 1983, 'Numerical Experiments with a One-dimensional Higher Order Turbulence Model: Simulations of the Wangara Day 33 Case', *Boundary-Layer Meteorol.* (accepted for publication).

Cotton, W. R. and Tripoli, G. J.: 1978, 'Cumulus Convection in Shear Flow Three-dimensional Numerical Experiments', *J. Atmos. Sci.* **35**, 1503–1521.

Deardorff, J. W.: 1980a, 'Cloud Top Entrainment Instability', *J. Atmos. Sci.* **31**, 131–147.

Deardorff, J. W.: 1980b, 'Stratocumulus-capped Mixed Layer Derived from a Three-dimensional Model', *Boundary-Layer Meteorol.* **18**, 495–527.

Herman, G. and Goody, R.: 1976, 'Formation and Persistence of Summertime Arctic Stratus Clouds', *J. Atmos. Sci.* **33**, 1537–1553.

Kaimal, J. C., Wyngaard, J. C., Haugen, D. A., Coté, O. R., Izumi, Y., Caughey, S. J., and Readings, C. J.: 1976, 'Turbulence Structure in the Convective Boundary Layer', *J. Atmos. Sci.* **33**, 2152–2169.

Klemp, J. B. and Wilhelmson, R. B.: 1978, 'The Simulation of Three-dimensional Convective Storm Dynamics', *J. Atmos Sci.* **35**, 1070–1096.

Lacis, A. A. and Hansen, J.: 1974, 'A Parameterization for the Absorption of Solar Radiation in Earth's Atmosphere', *J. Atmos. Sci.* **31**, 118–133.

Lilly, D. K.: 1968, 'Models of Cloud-topped Mixed Layers under Strong Inversion', *Quart. J. Roy. Meteorol. Soc.* **94**, 292–309.

Manton, M. J. and Cotton, W. R.: 1977, 'Formulation of Approximate Equations for Modeling Moist Deep Convection on the Mesoscale', Atmospheric Science Paper No. 266, Dept. of Atmos. Sci., Colorado State University.

Mellor, G. L.: 1977, 'The Gaussian Cloud Model Relations', *J. Atmos. Sci.* **34**, 356–358.

Neumann, G. and Pierson, Jr., W. J.: 1966, *Principles of Physical Oceanography*, Prentice-Hall, Englewood Cliffs, NJ.

Noonkester, V. R.: 1979, 'Coastal Marine Fog in Southern California', *Mon. Wea. Rev.* **107**, 830–851.

Oliver, D. A., Lewellen, W. S., and Williamson, G. G.: 1978, 'The Interaction Between Turbulent and Radiative Transport in the Development of Fog and Low-level Stratus', *J. Atmos. Sci.* **35**, 301–316.

Orville, H. D. and Kopp, F. J.: 1977, 'Numerical Simulation of the Life History of a Hailstorm', *J. Atmos. Sci.* **34**, 1596–1618.

Randall, D. A.: 1980, 'Conditional Instability of the First Kind Upside-down', *J. Atmos. Sci.* **37**, 125–130.

Rodgers, C. D.: 1967, 'The Use of Emissivity in Atmospheric Radiation Circulations', *Quart. J. Roy. Meteorol. Soc.* **93**, 43–54.

Schubert, W. H., Wakefield, J. S., Steinen, E. J., and Cox, S. K.: 1979, 'Marine Stratocumulus Convection. Part I: Governing Equations and Horizontally Homogeneous Solutions', *J. Atmos. Sci.* **36**, 1286–1307.

Sommeria, G., and Deardorff, J. W.: 1977, 'Subgrid-scale Condensation in Models of Nonprecipitating Clouds', *J. Atmos. Sci.* **34**, 344–355.

Stephens, G. L.: 1977, 'The Transfer of Radiation in Cloudy Atmosphere', Ph.D. Thesis, Meteorology Dept., University of Melbourne.

Stephens, G. L.: 1978, 'Radiation Profiles in Extended Water Clouds, Part II', *J. Atmos. Sci.* **35**, 2123–2132.

Stephens, G. L. and Webster, P. J.: 1979, 'Sensitivity of Radiative Forcing to Variable Cloud and Moisture', *J. Atmos. Sci.* **36**, 1542–1556.

Sun, W.-Y. and Ogura, Y.: 1980, 'Modeling the Evolution of Convective Planetary Boundary Layer', *J. Atmos. Sci.* **37**, 1558–1572.

Tripoli, G. J. and Cotton, W. R.: 1982, 'The Colorado State University Three-Dimensional Cloud/Mesoscale Model – 1981. Part I – General Theoretical Framework and Sensitivity Experiments', to be published in *J. de Rech. Atmos.*

Yamamoto, G.: 1962, 'Direct Absorption of Solar Radiation by Atmospheric Water Vapor, Carbon Dioxide and Molecular Oxygen', *J. Atmos. Sci.* **19**, 182–188.

Zeman, O. and Lumley, J.: 1976, 'Modeling Buoyancy Driven Mixed Layers', *J. Atmos. Sci.* **33**, 1974–1988.